Journal of Solid State Chemistry 185 (2012) 245–252

Contents lists available at SciVerse ScienceDirect

Journal of Solid State Chemistry

journal homepage: www.elsevier.com/locate/jssc

# One-dimensional $WO_3$ and its hydrate: One-step synthesis, structural and spectroscopic characterization

Kingsley O. Iwu [a,**], Augustinas Galeckas [b], Protima Rauwel [c], Andrej Y. Kuznetsov [b], Truls Norby [a,*]

[a] Department of Chemistry, University of Oslo, Centre for Materials Science and Nanotechnology, FERMiO, Gaustadalleen 21, NO-0349 Oslo, Norway
[b] Department of Physics, University of Oslo, Centre for Materials Science and Nanotechnology, P.O. Box 1048 Blindern, NO-0316 Oslo, Norway
[c] Centre for Materials Science and Nanotechnology, University of Oslo, P.O. Box 1126 Blindern, NO-0318 Oslo, Norway

ARTICLE INFO

*Article history:*
Received 5 October 2011
Accepted 2 November 2011
Available online 19 November 2011

*Keywords:*
Phase purity
Nanorods
Redshift
$W^{5+}$
Bandgap
Defect protons

ABSTRACT

We report on a one-step hydrothermal growth of one-dimensional (1D) $WO_3$ nanostructures, using urea as 1D growth-directing agent and a precursor free of metals other than tungsten. By decreasing the pH of the starting solution, the size of the nanostructures was reduced significantly, this development being accompanied by the realization of phase pure hexagonal $WO_3$ nanorods (elimination of monoclinic impurity phase) and a red shift in optical absorption edge. Surface analyses indicated the presence of reduced tungsten species in the $WO_3$ nanostructures, which increased two-fold in a hydrated $WO_3$ phase obtained with further decrease in pH. We suggest that oxygen vacancies are responsible for this defect state in $WO_3$, while protons are responsible or contribute significantly to the same in the hydrated phase.



## 1. Introduction

Tungsten trioxide ($WO_3$) has been widely investigated for applications in gas sensing [1], photoelectrochemical water splitting [2], photocatalytic decomposition of harmful organics [3], including human pathogens [4], and as a host material for cation intercalation-with application in electrochromic windows [5], lithium ion battery [6], and visible light transmitting/near infra red absorbing filter [7]. Although less studied than the anhydrous oxide, the hydrates ($WO_3 \cdot nH_2O$) have been investigated for application in electrochromism/lithium ion intercalation [8], proton conductivity [9], and hydrogen sensing [10]

Hydrothermal [5,11] and solvothermal [3,12] syntheses are two common methods for the preparation of 1D tungsten oxide. While the latter typically relies on the use of air-sensitive and volatile $WCl_6$ as a precursor, the hydrothermal route is more versatile because it can use a variety of precursors that are less toxic and easier to handle. However, all the hydrothermal preparations cited above utilize metal salts as 1D growth-directing agent, and/or precursors containing metals. This implies the possibility of having traces of unwanted non-volatile species in the final product. Indeed, alkali metal atoms have been reported to remain in hexagonal $WO_3$ ($h$-$WO_3$) prepared by hydrothermal synthesis [13], and this effect has also been observed in our experiments (unpublished).

In order to circumvent this problem in the present work, we have used ammonium paratungstate, APT [$(NH_4)_{10}W_{12}O_{41}(5H_2O)$], as a precursor and urea ($CH_4N_2O$) as 1D growth-directing agent, considering its propensity for forming strong and persistent 1D hydrogen bonds [14]. A heptahydrate form of the precursor has been used to prepare $h$-$WO_3$ nanorods [15]. However, the procedure involved a 7-day hydrothermal synthesis besides two additional hours-long steps of precursor preparation/modification. We also report on the control of the size and optical absorption properties of the resulting $WO_3$ nanostructures and variation in the concentration and source of reduced tungsten state between $WO_3$ and its hydrate.

## 2. Experimental

### 2.1. Materials synthesis

A standard solution (pH ~ 2.1) was prepared by dissolving 18 mg of APT and 132 mg of urea in 20 ml aqueous solution of acetic acid (20 vol%). The solution was heated at 180 °C for 12 h in a 40 ml Teflon-lined autoclave. After allowing the autoclave to cool down to room temperature, the product was isolated by centrifugation, washed twice with deionized water, once with

* Corresponding author (Post-publication). Fax: +47 22840651.
** Corresponding author (Pre-publication). Fax: +47 22840651.
*E-mail addresses:* k.o.iwu@smn.uio.no (K.O. Iwu), augustinas.galeckas@fys.uio.no (A. Galeckas), protima.singh@fys.uio.no (P. Rauwel), andrej.kuznetsov@fys.uio.no (A.Y. Kuznetsov), truls.norby@kjemi.uio.no (T. Norby).

0022-4596/$ - see front matter © 2011 Elsevier Inc. All rights reserved.
doi:10.1016/j.jssc.2011.11.001

isopropanol, and finally dried over silica gel. Experiments with varying amounts of urea were also carried out. Using the standard solution as a basis, various concentrations of HCl were employed to study the effect of pH on the hydrothermal products. Post-synthesis annealing was done at 380 °C for 1 h (ramp rate ~1 °C/min).

### 2.2. Materials characterization

Unless otherwise indicated, samples for characterization were prepared by dropping isopropanol solutions of the dry products on suitable substrates and drying on a hot plate maintained at 90 °C. The morphology of the products was investigated with a FEI Quanta 200 FEG-ESEM scanning electron microscope (SEM). (High Resolution) Transmission Electron Microscopy ((HR)TEM) studies were carried with a Jeol 2010F and a FEI Technai 20, both operating at 200 kV, and a 80-300 FEI Titan fitted with a $C_s$ corrector, operating at 300 kV and disposing a point to point resolution of 0.8 Å. X-ray diffraction (XRD) patterns were obtained with a Bruker D5000 XRD instrument equipped with a Braun position sensitive detector, with Cu $K\alpha_1$ radiation selected by a Ge (1 1 1) monochromator. Optical properties of the samples were investigated at room temperature by means of diffuse reflectance spectroscopy (DRS) using a ThermoScientific EVO-600 UV–vis spectrophotometer. The band gap energies and the dominant type of optical transitions were determined using standard Kubelka–Munk [16] and Tauc [17] treatment of the DRS spectra. Diffuse reflectance infrared Fourier transform spectroscopy (DRIFTS) measurements were done using a Perkin Elmer 2000 FT-IR spectrophotometer, with diffuse reflectance (DR) provided by a HARRICK DR accessory. The DRIFTS sample was a pulverized mixture of the silica dried product (7%) and KBr. Blank KBR measurements were done at all temperatures and the spectra subtracted from those of the sample. X-ray photoelectron spectroscopy (XPS) analyses were carried out with a Kratos Axis Ultra$^{DLD}$ XP spectrometer. The x-ray source was monochromatic Al $K\alpha$ radiation. For energy referencing, the W $4f_{7/2}$ of $W^{+6}$ peak was chosen and was set to 35.7 eV binding energy (BE).

## 3. Results and discussion

### 3.1. Effect of urea

SEM images of the products prepared with different amounts of urea are presented in Fig. 1a–d. The product prepared without urea consists of needle- and sheet-like nanostructures in addition to micron-sized structures. In contrast, a rod-like morphology with lengths of up to 2 μm and diameters ranging from 60 to 180 nm was obtained upon employing different amounts of urea. The rods prepared with 72 mg urea appear stunted while higher urea concentration products gave more uniform rods (slightly better size uniformity for 102 mg urea rods compared to 132 mg ones).

As shown in Fig. 2, the XRD patterns of the nanostructures prepared with urea are similar and matching to hexagonal $WO_3$ ($h$-$WO_3$, JCPDS 85-2459), while the pattern of the irregular products obtained without urea corresponds to monoclinic $WO_3$ ($m$-$WO_3$, JCPDS 83-0950) and orthorhombic $WO_3 \cdot (1/3)H_2O$ ($o$-$WO_3 \cdot (1/3)H_2O$, JCPDS 72-0199), with the former appearing dominant. These results demonstrate that 1D $WO_3$ free of metals other than tungsten can be obtained from APT in a one-step synthesis.

TEM studies were performed on the 132 mg urea product as a representative sample of the products prepared with urea. Fig. 3a shows a low magnification image giving a global view of the rods, some of which are not smooth at the ends and appear to taper off. Their selected area electron diffraction (SAED) pattern in the inset

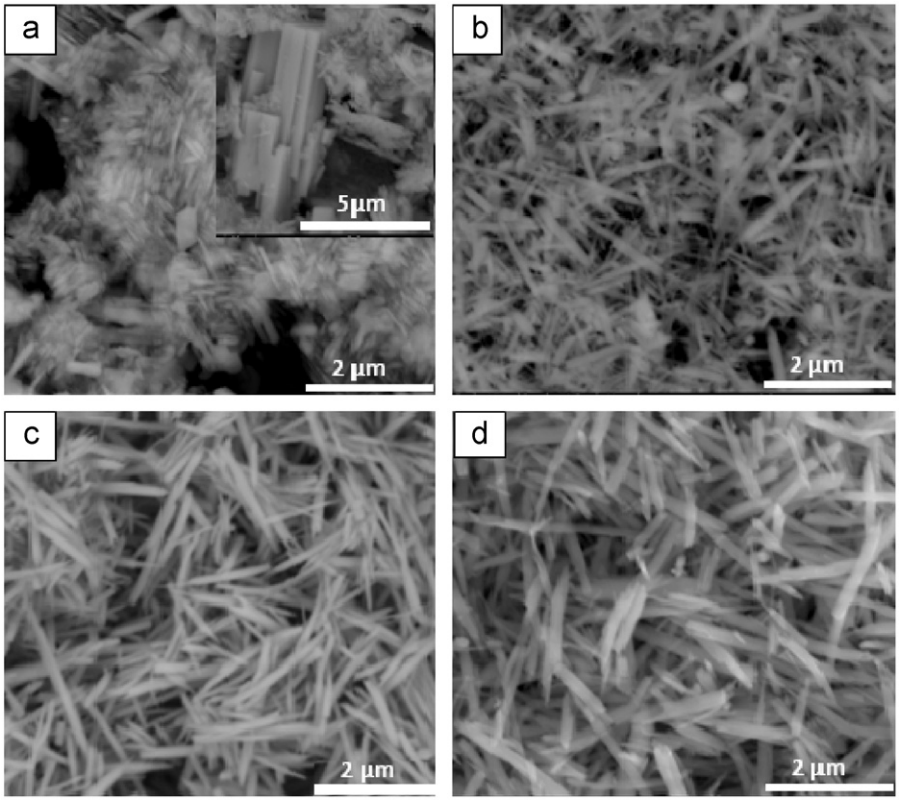


**Fig. 1.** SEM images of hydrothermal products prepared with different amounts of urea: (a) 0 mg, (b) 72 mg, (c) 102 mg, and (d) 132 mg.

corresponds to the $h$-$WO_3$ phase with space group $P6/mmm$ and lattice parameters $a=7.298$ Å and $c=3.899$ Å. A higher magnification TEM image of a rough end of a rod presented in Fig. 3b suggests that it is composed of smaller rods, i.e. individual rods are formed by an aggregate of nanorods growing together as a unit. This observation has been reported elsewhere [18]. The rough ends are probably due to uneven termination of the nanorod growth. An HRTEM image of the area of the rod delimited by a circle in Fig. 3b is shown in Fig. 3c. The rod is $m$-$WO_3$ and this monoclinic phase was not visible in the SAED pattern, indicating a minority phase of space group $P21/c$ oriented along the [001] zone axis with lattice parameters $a=7.306$ Å, $b=7.540$ Å, $c=7.692$ Å, $\beta=90.88$. The inset gives the plane spacings: $d_{200}=3.76$ Å and $d_{020}=3.65$ Å.

### 3.2. Effect of HCl and pH

The pH of the standard solution (132 mg urea, 0 M HCl) was varied in order to investigate its effect on the hydrothermal products. A few observations are noteworthy. At low molar concentrations of HCl (0.05 and 0.12 M), the XRD patterns of the resulting products (Fig. 4) are similar and matching to $h$-$WO_3$ (JCPDS 85-2495), just like the product from 0 M HCl. In comparison with the XRD pattern of the latter, however, a general minor shift of the peaks to the right and also an increased intensity of several reflections relative to that at $2\theta \approx 28^\circ$ can be observed. As presented in Fig. 4, further increase in the concentration of HCl to 0.20 M led to the formation of $o$-$WO_3 \cdot (1/3)H_2O$ (JCPDS 72-0199) and a mixture of $m$-$WO_3$ and $o$-$WO_3 \cdot (1/3)H_2O$ at 0.30 M. Finally, 0.50 M HCl yielded $m$-$WO_3$ (JCPDS 75-2072, Fig. 1 of supplementary information).

SEM images presented in Fig. 5 highlight the morphological evolution of the hydrothermal products with varying HCl concentration. The characteristic dimensions of $WO_3$ rods decrease significantly down to about 15–30 nm × 600–700 nm for 0.12 M HCl compared to about 100–180 nm × 0.50–1.9 μm for 0 M HCl (Fig. 5a–c), with the nanorods from the former assembled into spherical bundles. Such decrease in size could be beneficial for practical purposes by providing a shorter travel path for intercalated species or photo-excited charge carriers as well as for reducing the amount of material to be used in a device assembly. A decrease in the size of hydrothermal $WO_3$ nanorods with decreasing pH has been observed but, unlike the situation in our case, it was accompanied by strong agglomeration [19]. Distinct 1D morphology appeared lost when products containing hydrated $WO_3$ were obtained with 0.20 M and 0.30 M HCl (Fig. 5d–e). While their SEM images indicate the presence of nanostructures, 0.30 M HCl, in addition, contains some micron-sized sheets. Finally, 0.50 M HCl gave only micron-sized sheets and blocks of $m$-$WO_3$ (Fig. 5f).

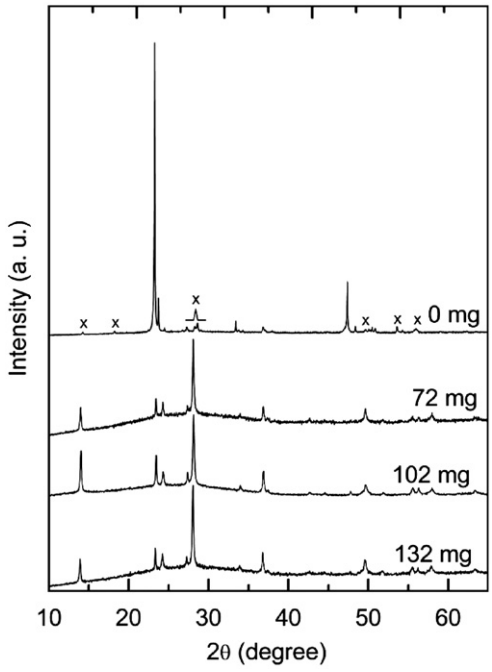


**Fig. 2.** XRD patterns of hydrothermal products prepared with varying amounts of urea. Peaks belonging exclusively to $o$-$WO_3 \cdot (1/3)H_2O$ in 0 mg urea are indicated with x.

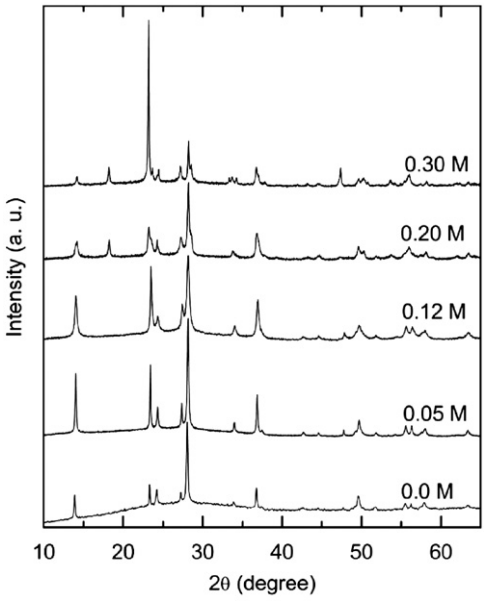


**Fig. 4.** XRD of samples prepared by adjusting the pH of the standard solution (0.0 M HCl) with varying concentrations of HCl.

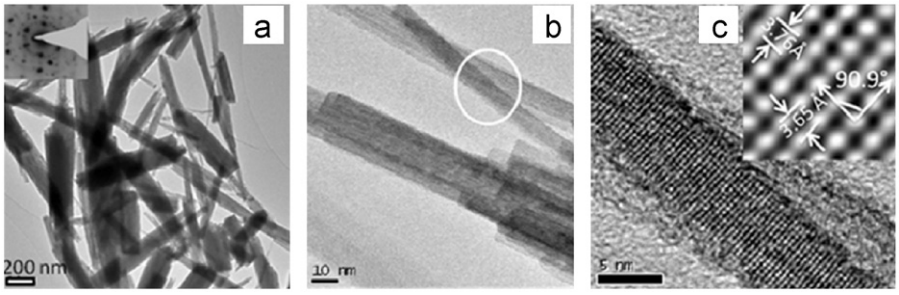


**Fig. 3.** (a)TEM image of $WO_3$ nanostructures prepared with 132 mg urea, with the SAED pattern in the inset, (b) higher magnification image of a rough end of a rod, and (c) HRTEM image of the circled part in (b), the inset is a magnified part providing the interplanar distances of the $m$-$WO_3$ phase.

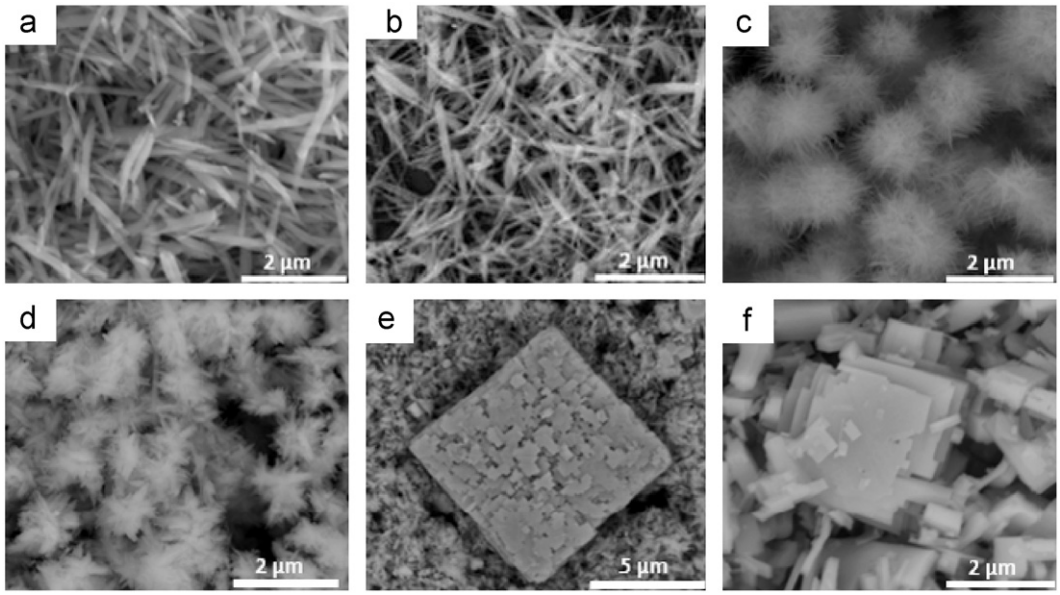


**Fig. 5.** SEM images of hydrothermal products prepared with varying concentration of HCl: (a) 0.0 M, (b) 0.05 M, (c) 0.12 M, (d) 0.20 M, (e) 0.30 M, and (f) 0.50 M. Microsheets, when obtained, tend to self-assembly; the near perfect square arrangement of jigsaw-like sheets from 0.30 M HCl synthesis being the best example witnessed.

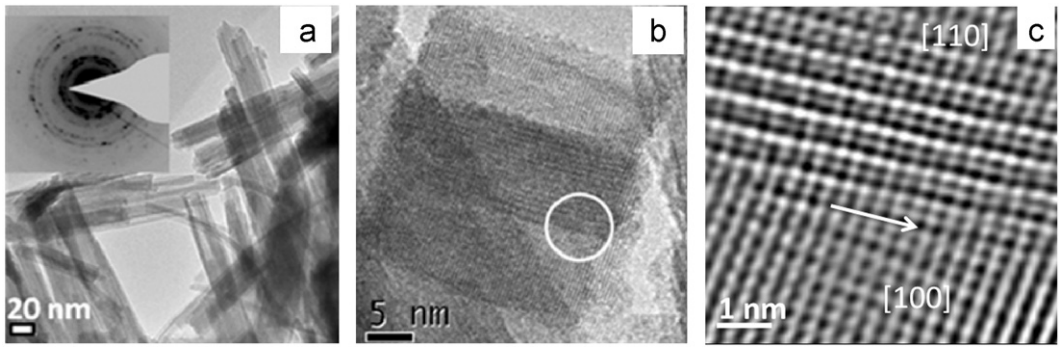


**Fig. 6.** (a) TEM image of $WO_3$ nanorods prepared with 0.12 M HCl, the inset is the corresponding SAED pattern, (b) HRTEM image of three 0.12 M HCl nanorods forming a platelet, and (c) stacking faults from the circled region in (b).

The XRD and SEM results for 0.30 M HCl product are generally similar to those of the irregular product obtained without urea. Until 0.20 M HCl, the XRD reflection at $2\theta \approx 28^\circ$ remained the most intense. However, at 0.30 M HCl, the highest intensity reflection is seen at $2\theta \approx 23^\circ$, which is the same for the irregular products synthesized without urea (compare 0.30 M HCl XRD pattern in Fig. 4 with that of 0 mg urea in Fig. 2).

(HR)TEM analyses were carried out on the nanostructures prepared with 0.12 M and 0.20 M HCl which have been identified by XRD as *h*-$WO_3$ and *o*-$WO_3 \cdot (1/3)H_2O$, respectively. As shown in Fig. 6a, some nanorods from the synthesis with 0.12 M HCl are, like the 0 M HCl case, composed of smaller nanorods. Their SAED pattern as presented in the inset shows only reflections corresponding to *h*-$WO_3$. Fig. 6b is a HRTEM image of a platelet from the 0.12 M HCl synthesis formed by three nanorods growing with a certain epitaxy. The region specified by the circle has been magnified in Fig. 6c to show two different orientations of *h*-$WO_3$ sharing a common grain boundary via a stacking fault. No other $WO_3$ polymorph was detected by HRTEM. This indicates that besides inducing a reduction in the dimension of the rods, increased HCl concentration also leads to phase pure *h*-$WO_3$. 1D *h*-$WO_3$ has been prepared at a comparable pH to ours [11a,b], and also at higher pH value of 2.0 [5]. TEM study carried out on the 0.20 M HCl product shows a "star-like" arrangement of bundles of agglomerated nanorods (Fig. 7a–b). According to the SAED pattern in the inset of Fig. 7a and in agreement with XRD, they are preferentially oriented along the [111] zone axis of the *o*-$WO_3 \cdot (1/3)H_2O$ structure with space group *Fmm*2 and lattice parameters $a=0.7359$ Å, $b=1.2513$ Å, $c=0.7704$ Å. The HRTEM image in Fig. 7c, oriented along the [100] zone axis, provides d-spacings of 6.26 Å and 3.85 Å, corresponding to the (0 2 0) and (0 0 2) reflections of *o*-$WO_3 \cdot (1/3)H_2O$, respectively. Impurity *m*-$WO_3$ (not shown) and *h*-$WO_3$ (Fig. 7d) were also observed. Moreover, stacking faults were clearly observed in the *h*-$WO_3$ phase (not shown), which could be due to the presence of planar defects induced by structural water [20]. Even though *o*-$WO_3 \cdot (1/3)H_2O$ and *h*-$WO_3$ structures are pseudomorphs [20], we think that the quantity of crystal water in the impurity *h*-$WO_3$ phase here may have been insufficient to engender the hexagonal to orthorhombic transformation. Therefore, for the sake of simplicity, we will refer to the 0.20 M HCl product as *o*-$WO_3 \cdot (1/3)H_2O$ with impurity *m*-$WO_3$.

Based on the results obtained, the effects of urea and pH on the hydrothermal products can be outlined as follows. As a starting point, a highly irregular product consisting of *m*-$WO_3$ and *o*-$WO_3 \cdot (1/3)H_2O$ is obtained without urea and HCl. Upon addition of urea, predominantly 1D *h*-$WO_3$ nanostructures with traces of secondary *m*-$WO_3$ are derived. By combining both urea

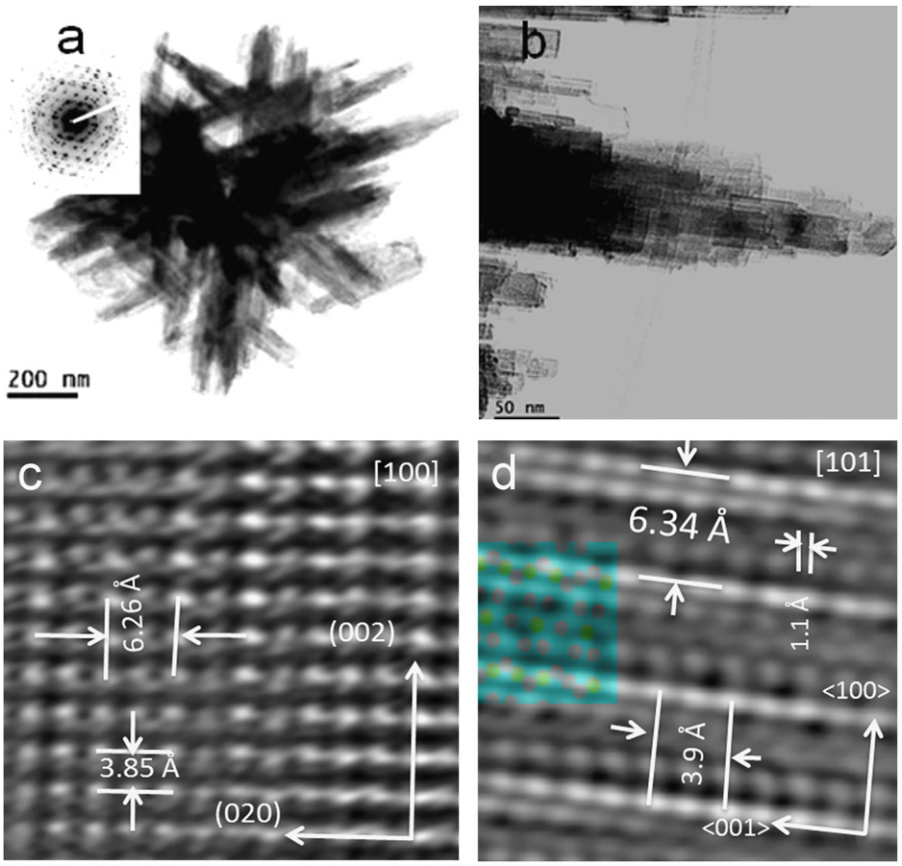


**Fig. 7.** (a) TEM image of 0.20 M HCl product, the inset is the SAED pattern, (b) higher magnification image of a protrusion in (a), (c) a HRTEM of the main *o*-$WO_3 \cdot (1/3)H_2O$ phase, (d) a HRTEM image of the minority *h*-$WO_3$, the inset is a superimposition of atoms arranged along the ⟨1 0 1⟩ zone axis. Green: W atoms, Pink: O atoms. (For interpretation of the references to colour in this figure legend, the reader is referred to the web version of this article.)

and HCl, a phase-pure *h*-$WO_3$ can be obtained, along with a considerable decrease in the dimensions of the rods. Upon further increase in the concentration of HCl to 0.30 M, we end up with a situation similar to the starting point. The pH induced size reduction could be explained from the viewpoint of complexation and nucleation. Carboxylic acid can chelate tungsten via the OH of the carboxylic group, and this can be inhibited by deprotonation of the carboxylic OH [21]. The reversible deprotonation reaction can be favorably driven backwards by excess $H^+$ ions. If we assume that the path to nucleation and 1D growth starts with the complexation step (synthesis with 0.05 M HCl and 132 mg urea but without acetic acid did not yield any precipitate), we can infer that there will be more growing nuclei with increase in HCl concentration. This in turn will lead to smaller and increased number of rods. Further increase in the concentration of HCl probably led to more direct interaction between the tungstate species and protons, leading to a deviation from the 1D growth reaction pathway [22].

### 3.3. XPS analysis

For all products studied by XPS, no evidence of substitutional nitrogen [23] or carbon [24] doping was found. Fig. 8a is the W 4*f* spectrum of the mainly *h*-$WO_3$ nanostructure prepared with 132 mg urea (0 M HCl). In addition to $W^{6+}$ state indicated by the doublets at BE 35.7 and 37.8 eV [25], the smaller peak at BE 34.3 eV and its deconvoluted pair at BE 36.4 eV are indicative of $W^{5+}$ [26]. The concentration of $W^{5+}$ with respect to $(W^{5+})+(W^{6+})$ was calculated to be 1.4%. Two other anhydrous oxides – 0.12 M HCl (*h*-$WO_3$ nanorods) and 0.50 M HCl (*m*-$WO_3$ microsheets) – have $W^{5+}$ contents of 1.2% and 1.5%, respectively (spectra not shown). In previous XPS studies of hydrothermal $WO_3$ [11a,27,28], no evidence of $W^{5+}$ state was found. These contents of $W^{5+}$ can be attributed to the presence of oxygen vacancies and their compensating electrons [29]. The concentration of the former in an oxygen deficient oxide can be shown to be proportional to $pO_2^{-1/6} \exp(-\Delta H/kT)$ [30], where $\Delta H$ stands for the enthalpy of formation of an oxygen vacancy and two electrons. The exponential dependence of the concentration of oxygen vacancies on temperature may have favored their formation in our hydrothermal synthesis.

The W 4*f* core level spectrum (Fig. 8b) of the nanorods prepared with 0.20 M HCl (*o*-$WO_3 \cdot (1/3)H_2O$) indicated a $W^{5+}$ content of 2.8%, which is roughly twice the concentration in the three anhydrous oxides above. This trend was also observed in another $WO_3 \cdot (1/3)H_2O$ and $WO_3$ samples prepared with a different carboxylic acid (subject of further studies). Besides, the irregular product obtained with 0 mg urea (with a minority *o*-$WO_3 \cdot (1/3)H_2O$ phase) has a $W^{5+}$ content of 2.3% (spectrum shown in Fig. 2 of supporting information), which is significantly higher than the concentration in the anhydrous products. These results indicate a correlation between water (of hydration) and higher $W^{5+}$ concentration in our study. In contrast to our finding, Zhou et al. found no reduced tungsten state in hydrothermal *o*-$WO_3 \cdot (1/3)H_2O$, though they reported a significant concentration of reduced molybdenum when they substituted tungsten with molybdenum [31].

In order to gain further insight into the nature of the defects in the hydrated oxide, an annealed sample was analyzed, and for comparison, that of 0 M HCl (non-hydrated $WO_3$) also. The $W^{5+}$ content increased from 1.4% to 2.1% for $WO_3$. This indicates an increased concentration of ionized oxygen vacancies with increasing temperature, which is in agreement with its dependence on

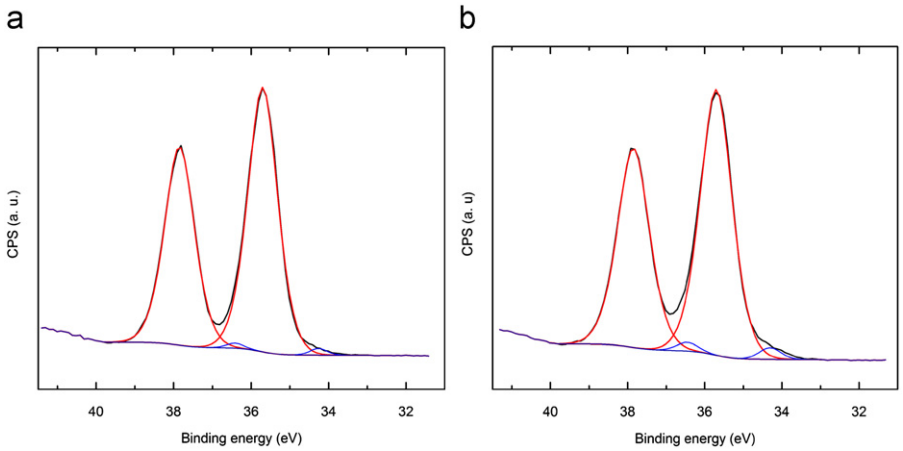


**Fig. 8.** W 4*f* XPS spectra of nanostructures prepared with (a) 0.0 M HCl ($WO_3$), and (b) 0.20 M HCl ($o$-$WO_3 \cdot (1/3)H_2O$).

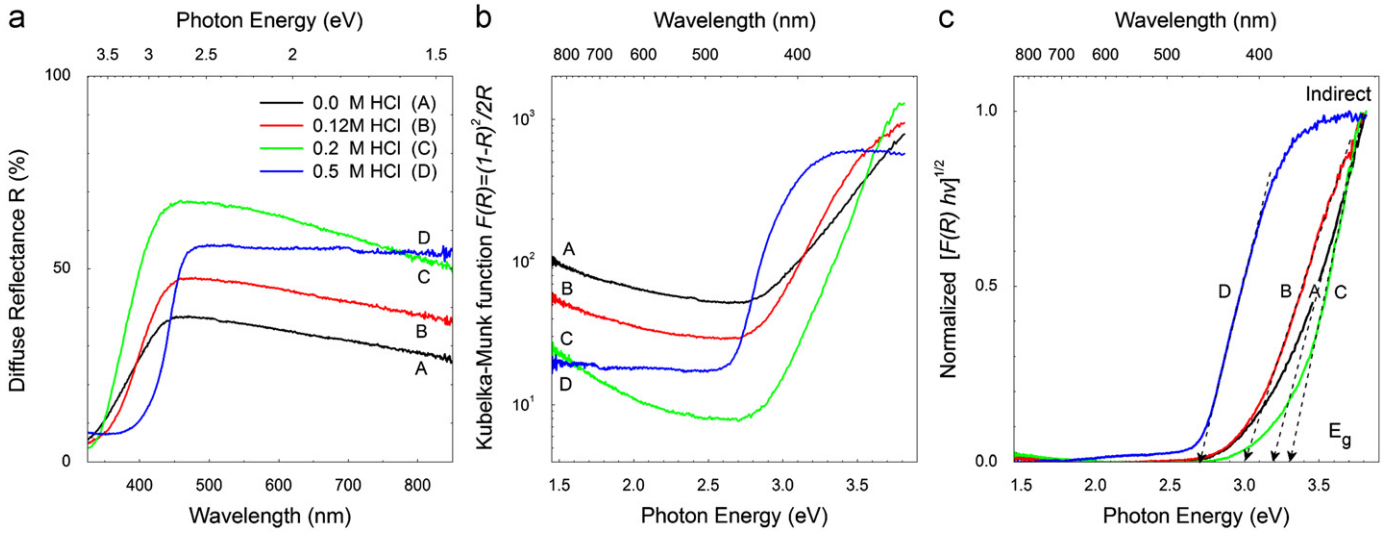


**Fig. 9.** Diffuse reflectance UV–vis spectra of hydrothermal samples prepared with different HCl concentration (a), corresponding Kubelka–Munk functions (b) and normalized Tauc plots (c), assuming indirect optical transitions.

temperature. On the contrary, the $W^{5+}$ content decreased for $WO_3 \cdot (1/3)H_2O$, from 2.8% down to 1.6%, accompanied by a phase transformation to $WO_3$ as indicated by the XRD patterns in Fig. 3 of supporting information and the DRIFTS spectra in Fig. 10. This trend, which suggests the presence of another positively charged defect other than oxygen vacancy, was also observed in the $WO_3 \cdot (1/3)H_2O$ and $WO_3$ samples from a different carboxylic acid. Unlike the report by Daniel et al. [32], the DRIFTS or IR spectra of our $WO_3 \cdot (1/3)H_2O$ shows a stronger intensity of adsorbed water compared to the structural water, with the former persisting at higher temperatures (above 400 °C) after the latter has been completely removed at around 350 °C. This adsorbed water, according to Daniel et al., is thought to react with surface oxygen atoms to form OH groups.

In view of our results, it is reasonable to assume that defect protons are responsible or significantly contributory to the concentration of $W^{5+}$ in $WO_3 \cdot (1/3)H_2O$ according to the hydration reaction:

$$H_2O\ (g) + 2O^{2-}(s) = 2OH^-(s) + 2e^- + (1/2)O_2\ (g)$$

In fact, enhanced proton uptake in $WO_3 \cdot nH_2O$ in comparison to $WO_3$ has been attributed to the presence of lattice water [10], and $WO_3 \cdot (1/3)H_2O$ in particular is reported to have a strong affinity for water [32]. In general, the presence of defect electrons in our samples is expected to enhance their applications, for example in conductivity-based gas sensing [33] and electrochromic/photochromic devices [34].

### 3.4. $WO_3$ band gap evolution

Diffuse reflectance UV–vis spectroscopy was applied to study optical properties of $WO_3$. The bandgap variation was estimated from the position of the absorption edge, which in turn was determined from the corresponding Tauc plot, i.e. modified Kubelka–Munk function versus photon energy, assuming indirect origin of the optical transitions. Fig. 9 illustrates this procedure applied for estimation of the bandgap.

The band gap estimated for the nanostructures (mainly $h$-$WO_3$) prepared with 132 mg urea (0 M HCl) is ~3.20 eV (Fig. 9). The same value was obtained for the nanostructures prepared with 72 and 102 mg urea (spectra not shown). When pH was reduced with 132 mg urea as basis, we observed not only a decrease in the dimensions of $WO_3$ nanostructures but also a red shift in absorption. The band gap decreased to 3.0 eV for 0.12 M HCl nanorods (Fig. 9a–c), which incidentally is the product with phase pure $h$-$WO_3$ (no impurity $m$-$WO_3$). This red-shift in absorption cannot be attributed to the elimination of impurity monoclinic phase, considering that our

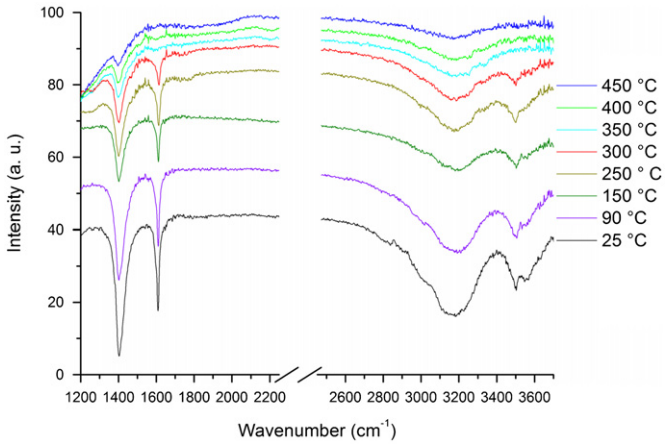


**Fig. 10.** DRIFTS spectra of $WO_3 \cdot (1/3)H_2O$ at different temperatures in ambient air. The peaks centered at 1405 $cm^{-1}$ and 3200 $cm^{-1}$ are due to adsorbed water while those at 1610 $cm^{-1}$ and 3500 $cm^{-1}$ are ascribed to the structural water [32]. The region from 2250 to 2450 $cm^{-1}$ that has been cut-off corresponds to $CO_2$ contamination.

experimental results indicate lower band gap of 2.7 eV for *m*-$WO_3$ (0.50 M HCl), also shown in Fig. 9. In literature, *h*-$WO_3$ is assigned a band gap value of 3.30 eV [35] whereas *m*-$WO_3$ is associated with lower band gap values in the range from 2.50 to 2.75 eV [24,36].

Regarding the source of the red-shift in optical absorption, XPS results have already eliminated the possibility of substitutional carbon or nitrogen doping. Raftery et al. [24] suggested that carbon interstitial atoms could be responsible for a decrease in absorption edge of $WO_3$. However, the calculated concentrations of all carbon and nitrogen species present in the XPS spectra did not provide a clear evidence in that direction. The small difference in the concentration of $W^{5+}$ between 0 M and 0.12 M HCl nanostructures could be the reason for this shift in absorption edge; increased concentration of oxygen vacancies is said to increase the absorption edge of $WO_3$ [37]. However, the lower band gap value of 0.50 M HCl product (*m*-$WO_3$), which has a $W^{5+}$ concentration similar to 0 M HCl, does not seem to support this argument in our case. It should be noted that this red shift in absorption is the complete opposite of what one would expect from quantum confinement effect in reduced-dimension structures. Although the reason for this red shift remains unclear at the moment, the demonstrated possibility to tune the absorption edge nonetheless might be of interest for some practical applications, for instance in the field of photovoltaics.

## 4. Conclusions

We have prepared $WO_3$ nanostructures in a straightforward manner, obtaining a single-phase ID *h*-$WO_3$ by adjusting the pH of the starting hydrothermal solution. This opens up the possibility for quick preparation of *h*-$WO_3$ nanorods using any aqueous tungstate solution without contamination from other metal cations. For the first time, we have also demonstrated the possibility to activate a reduction in size and red shift in absorption edge of $WO_3$ nanostructures simultaneously. Our synthetic approach also leads to the presence of defect states in the products. Further investigations on the defects and optical properties of $WO_3$ and its hydrate are ongoing.

## Acknowledgment

This work has been funded by the Research Council of Norway (RCN, RENERGI 191080 "Solid-State Photoelectrochemical Production of Hydrogen"). The authors thank Martin F. Sunding of Department of Physic, University of Oslo, for XPS experiments, and Professor Claus Jørgen Nielsen of Department of Chemistry, University of Oslo, for help with the DRIFTS experiment. The Centre for Electron Nanoscopy at the Technical University of Denmark is acknowledged for access to the Technai 20 and Cs corrected 80-300 FEI Titan TEM instruments.

## Appendix A. Supplementary materials

Supplementary data associated with this article can be found in the online version at doi:10.1016/j.jssc.2011.11.001.

## References

[1] (a) D.-S. Lee, S.-D. Han, J.-S. Huh, D.-D. Lee, Sensors and Actuators B: Chemical 60 (1999) 57–63;
(b) O.-u. Nimittrakoolchai, S. Supothina, Materials Chemistry and Physics 112 (2008) 270–274.
[2] (a) C. Santato, M. Odziemkowski, M. Ulmann, J. Augustynski, Journal of the American Chemical Society 123 (2001) 10639–10649;
(b) M. Bar, L. Weinhardt, B. Marsen, B. Cole, N. Gaillard, E. Miller, C. Heske, Applied Physics Letters 96 (2010) 032103–032107.
[3] Z.G. Zhao, M. Miyauchi, Angewandte Chemie International Edition 47 (2008) 7051–7055.
[4] D. Macphee, R. Wells, A. Kruth, M. Todd, T. Elmorsi, C. Smith, D. Pokrajac, N. Strachan, M. Mwinyhija, E. Scott-Emuakpor, S. Nissen, K. Killham, Desalination 248 (2009) 132–137.
[5] J. Wang, E. Khoo, P.S. Lee, J. Ma, The Journal of Physical Chemistry C 112 (2008) 14306–14312.
[6] N. Kumagai, N. Kumagai, Y. Umetzu, K. Tanno, J.P. Pereira-Ramos, Solid State Ionics 86–88 (1996) 1443–1449.
[7] H. Takeda, K. Adachi, Journal of the American Ceramic Society 90 (2007) 4059–4061.
[8] A. Bessiere, C. Marcel, M. Morcrette, J.M. Tarascon, V. Lucas, B. Viana, N. Baffier, Journal of Applied Physics 91 (2002) 1589–1594.
[9] Y.M. Li, M. Hibino, M. Miyayania, T. Kudo, Solid State Ionics 134 (2000) 271–279.
[10] K. Ito, T. Ohgami, Applied Physics Letters 60 (1992) 938–940.
[11] (a) S. Rajagopal, D. Nataraj, D. Mangalaraj, Y. Djaoued, J. Robichaud, O. Khyzhun, Nanoscale Research Letters 4 (2009) 1335–1342;
(b) H. Kai, et al., Journal of Physics D: Applied Physics 41 (2008) 155417;
(c) J. Zhang, J.-P. Tu, X.-H. Xia, X.-L. Wang, C.-D. Gu, Journal of Materials Chemistry 21 (2011) 5492–5498.
[12] C. Guo, S. Yin, P. Zhang, M. Yan, K. Adachi, T. Chonan, T. Sato, Journal of Materials Chemistry 20 (2010) 8227–8229.
[13] K.P. Reis, A. Ramanan, M.S. Whittingham, Chemistry of Materials 2 (1990) 219–221.
[14] R. Custelcean, Chemical Communications (2008) 295–307.
[15] H.A. Therese, J. Li, U. Kolb, W. Tremel, Solid State Sciences 7 (2005) 67–72.
[16] P. Kubelka, F. Munk, Zhurnal Tekhnicheskoi Fiziki 12 (1931) 593–601.
[17] J. Tauc, R. Grigorovici, A. Vancu, Physica Status Solidi 15 (1966) 627–637.
[18] R.-F. Mo, G.-Q. Jin, X.-Y. Guo, Materials Letters 61 (2007) 3787–3790.
[19] J. Wang, E. Khoo, P.S. Lee, J. Ma, The Journal of Physical Chemistry C 113 (2009) 9655–9658.
[20] B. Gerand, G. Nowogrocki, M. Figlarz, Journal of Solid State Chemistry 38 (1981) 312–320.
[21] T. Tanzawa, J. Schwartz, Organometallics 9 (1990) 3026–3027.
[22] S. Supothina, P. Seeharaj, S. Yoriya, M. Sriyudthsak, Ceramics International 33 (2007) 931–936.
[23] Y.-C. Nah, I. Paramasivam, R. Hahn, N.K. Shrestha, P. Schumki, Nanotechnology 21 (2010) 105704.
[24] Y. Sun, C.J. Murphy, K.R. Reyes-Gil, E.A. Reyes-Garcia, J.M. Thornton, N.A. Morris, D. Raftery, International Journal of Hydrogen Energy 34 (2009) 8476–8484.
[25] M. Ranjbar, A. Iraji zad, S. Mahdavi, Applied Physics A: Materials Science and Processing 92 (2008) 627–634.
[26] F. Di Gregorio, V. Keller, Journal of Catalysis 225 (2004) 45–55.
[27] R. Huirache-Acuña, F. Paraguay-Delgado, M.A. Albiter, J. Lara-Romero, R. Martínez-Sánchez, Materials Characterization 60 (2009) 932–937.
[28] A. Phuruangrat, D.J. Ham, S.J. Hong, S. Thongtem, J.S. Lee, Journal of Materials Chemistry 20 (2010) 1683–1690.
[29] E. Lassner, W.-D. Schubert, Tungsten Properties, Chemistry, Technology of the Element, Alloys, and Chemical Compounds, Kluwer Academic/Plenum Publishers, New York, 1999.
[30] P. Kofstad, Nonstoichiometry, Diffusion, and Electrical Conductivity in Binary Metal Oxides, John Wiley & Sons Inc., New York, 1972.
[31] L. Zhou, J. Zhu, M. Yu, X. Huang, Z. Li, Y. Wang, C. Yu, The Journal of Physical Chemistry C 114 (2010) 20947–20954.

[32] M.F. Daniel, B. Desbat, J.C. Lassegues, B. Gerand, M. Figlarz, Journal of Solid State Chemistry 67 (1987) 235–247.
[33] I. Jimenez, J. Arbiol, A. Cornet, J.R. Morante, Sensors Journal, IEEE 2 (2002) 329–335.
[34] A. Rougier, F. Portemer, A. Quédé, M. El Marssi, Applied Surface Science 153 (1999) 1–9.
[35] K. Huang, Q. Zhang, F. Yang, D. He, Nano Research 3 (2010) 281–287.
[36] (a) S. Berger, H. Tsuchiya, A. Ghicov, P. Schmuki, Applied Physics Letters 88 (2006) 203113–203119;
(b) F. Amano, D. Li, B. Ohtani, Chemical Communications 46 (2010) 2769–2771;
(c) B. Cole, B. Marsen, E. Miller, Y. Yan, B. To, K. Jones, M. Al-Jassim, The Journal of Physical Chemistry C 112 (2008) 5213–5220.
[37] S.K. Deb, Solar Energy Materials and Solar Cells 92 (2008) 245–258.